Development of a Nested Coastal Circulation Model: Boundary Error Reduction

S Nash and M Hartnett

College of Engineering & Informatics, National University of Ireland Galway

Corresponding Author: Dr. Stephen Nash

Tel: +353 91 493738

Fax: +353 91 494507

Email: stephen.nash@nuigalway.ie

Abstract

Numerical models have a valuable role to play in the sustainable management of coastal waters but accurate simulation of land-sea interactions, particularly in areas of complex coastlines, requires the use of high spatial resolutions. As a result, the computational cost of such models can become quite prohibitive. Nesting techniques offer a cost-effective solution to the spatial resolution problem by allowing specification of high spatial resolutions in limited areas, i.e. selective down-scaling. A one-way nested model was developed for simulation of tidal hydraulics in coastal waters. The nesting procedure was developed to reduce errors in the nested domain generated by the treatment of the nested open boundaries. Such 'boundary errors' are primarily caused by loss of mass and momentum due to non-conservative boundary schemes and/or inaccurate boundary data due to unsuitable nested boundary locations. In the first instance, high levels of conservation of mass and momentum are achieved by the use of a Dirichlet boundary condition and linear interpolation scheme for specification of nested boundary data, and by a nested boundary configuration incorporating ghost cells which, in effect, allows the formulation of open boundaries as 'internal boundaries'. In the second instance, a procedure for identification of suitable nested boundary locations ensures the level of error passed from the low resolution solution to the nested solution via the boundary prescription is low. Nested model functionality was verified for both experimental and natural test conditions. The nesting procedure was found to reduce boundary errors and produce highly accurate solutions for a fraction of the computational cost of high resolution single grid models.

Keywords: nested model; hydrodynamics; boundary errors; ghost cells; internal boundary.

1 Introduction

The problem of computational cost in oceanographic modelling is a perennial one. A main determinant of computational cost is spatial resolution. Higher resolution, while desirable for greater accuracy, often results in prohibitively high computational costs due to the large number of grid points. The problem is particularly challenging when modelling coastal waters as the irregularity of coastlines and the scale of the physical/chemical processes involved require high spatial resolutions. As a result, it is estimated that coastal shelf seas, while only occupying seven percent of the deep ocean by area, require 70 times the computer power of the deep ocean (Natural Environment Research Council, 2009). An additional related problem is the location of open boundaries such that their conditions will not adversely affect model predictions in the interior domain. This often necessitates a large computational domain, of which the area of interest (AOI) comprises only a small percentage.

The solution to the spatial resolution problem is the specification of high spatial resolution in areas of interest only and the use of lower resolution elsewhere, known as selective mesh refinement. The unstructured grid approach offers greater flexibility in selective mesh refinement over the traditional, structured grid approach. Despite this, structured grid models are still widely used (e.g. You et al., 2010; Olbert et al., 2012; Wang, 2012) and powerful solutions have been developed for refining the structured mesh when and where needed (see Deleersnijder and Lermusiaux (2008) for a review). One such solution, and the focus of this research, is grid nesting. This involves the embedding of a higher resolution grid (the child grid - CG) within a lower resolution grid (the parent grid - PG). Successive embedding of child grids can be used to obtain the desired degree of spatial resolution in an area of interest. The approach was first applied in oceanographic modelling by Spall and Robinson (1989) but its use is now well-established (e.g. Zhang, et al., 2007; Staneva et al., 2009; Ji, et al., 2011; Hasegawa et al., 2011; Shan et al., 2011).

Nesting approaches fall into one of two categories - one-way or two-way nesting. In one-way nesting, interaction between parent and child grids occurs in one direction only, from parent to child. The PG solution is used to provide boundary conditions to generate the CG solution but the CG solution cannot influence the PG solution. This approach is most commonly adopted for down-scaling (global-regional-local) applications where only the CG solution is of interest (e.g. Korres and Lascaratos, 2003; Leitão et al., 2005; Staneva et al., 2009; Holt et al., 2009; Ji et al., 2011; Janekovic, 2012; Wang, 2012). By comparison, two-way nesting (e.g. Barth el al., 2005; Debreu et al., 2012) allows interaction in two directions; the PG solution is used to provide boundary conditions to generate the CG solution and the CG solution is, in turn, used to improve the PG solution. The two-way approach is used in applications where features that develop in the CG may propagate outside of the CG domain; for example, when simulating the far-field impacts of tidal turbines (see Hasegawa (2011)).

The present model was developed to facilitate local down-scaling in coastal domains and a one-way nested approach was adopted accordingly.

While nested grid models offer a useful solution to the spatial resolution problem, they are not without their deficiencies. For example, there is an added computation time due to the solution of the model on both the parent and child grid(s). However, since the resolution of the parent grid is relatively coarse its computational cost should be quite low in relation to that of the child and the added computational cost to the nested model should therefore be only a small percentage of the overall cost. Of more importance is the potential for the generation of *boundary errors* in the nested solution. In a nested model, the PG prescribes flow to the CG via lateral boundary conditions (BCs). In this context, boundary errors are that part of the total error in the nested domain solution directly attributable to the imposed boundary conditions. Baumhefner and Perkey (1982) identified two main components of boundary errors in nested domains:

1) boundary formulation errors (BFEs), caused by the formulation of the BC
2) boundary specification errors (BSEs), caused by the specification of inaccurate boundary data

The response of a model domain interior is sensitive to the choice of BC and many studies have shown that different types of applied BC can lead to significantly different CG solutions (Palma and Matano, 1998; Marchesiello et al., 2001; Oddo and Pinardi, 2008; Mason et al., 2010). Such differences in CG solutions are a result of BFEs. BFEs occur when PG waves entering the CG are distorted as they pass through the boundary or when CG waves leaving the CG domain are reflected by the boundary (Garcia-Menendez and Odman (2011)). Distortion of incoming PG waves leads to conservation losses (Debreu and Blayo, 2008) and reflection of CG waves leads to energy build-up within the CG domain and possibly instability (Hertzfeld, 2009). Numerous studies have evaluated the performance of different BC schemes (clamped, relaxation, radiation and advection) in nested models (Blayo and Debreu, 2005; Cailleau et al., 2008; Lavelle and Thacker, 2008; Oddo and Pinardi, 2008; Herzfeld and Andrewartha, 2011) and it is a very active research area. The second component of boundary errors, BSEs, are a result of inaccuracies in the PG data specified at CG boundaries which then propagate into the interior solution of the CG domain (Herzfeld, 2009). Baumhefner and Perkey (1982) showed BSEs to account for 50% of the boundary errors in a nested grid solution but it is clear that if the PG solution is quite inaccurate then BSEs can swamp BFEs. BSEs can be minimised through careful location of CG boundaries such that local errors in the PG solution are low.

The focus of the present research is the reduction of both BFEs and BSEs in a one-way nested model. Here, we have developed a synchronous, nested hydrodynamic model for coastal waters that operates on a uniform rectilinear grid. Particular attention was placed on the design of the nested boundary to reduce the potential for generation of boundary errors. A ghost cell approach to the mathematical

formulation of the governing equations on the nested boundary was developed which internalises the nested open boundaries. Ghost cells are incorporated adjacent, but external, to the CG domain and improve conservation of mass and momentum at the boundary interfaces. The CG boundary condition (including interpolation operators) was designed to achieve high levels of conservation of mass and momentum at the boundary interface. Finally, a procedure for identifying optimal CG boundaries was developed to ensure that PG data assigned to CG boundaries is accurate. This paper describes the nesting approach implemented in the model with particular emphasis on the nested boundary and the reduction of boundary errors. Results are presented for applications to an idealised harbour, an experimental tidal basin and Galway Bay, a natural inlet located on the west of Ireland. The results (a) show how one can differentiate between BFEs and BSEs, (b) demonstrate the effectiveness of the nesting approach in reduction of these boundary errors, and (c) quantify the accuracy and computational efficiencies of the nested model.

2 The Nested Model

The nested model was developed from the hydrodynamic and solute transport model DIVAST (depth integrated velocity and solute transport) which is applicable to shallow coastal waters and has been widely used and validated (e.g. Nash et al. (2010); Hartnett et al. (2012)). It is a two-dimensional, depth-averaged, finite difference model with coupled hydrodynamic and solute transport modules. For model development, the modules were decoupled and the hydrodynamic module alone used. The model solves the depth integrated Navier-Stokes equations and includes the effects of local and advective accelerations, the rotation of the earth, free surface pressure gradients, wind action, bed resistance and a simple mixing length turbulence model. Full details of the hydrodynamic formulations are given in Falconer et al. (1984).

The governing differential equations for conservation of mass and momentum are solved using a finite difference scheme based upon the *Alternating Direction Implicit* (ADI) technique which involves the sub-division of each timestep into two half-timesteps. This allows a two-dimensional implicit scheme to be applied but considering only one dimension implicitly for each half-timestep. A space-staggered orthogonal grid system is used with water elevation (ζ) discretised at the centre of the grid cell and velocity components (U and V), volumetric flux components (q_x and q_y) and water depths (H_x and H_y) discretised at the centre of the cell sides (Figure 1). The model contains a robust flooding and drying routine (see Falconer and Chen (1991) for details) allowing intertidal areas to be adequately simulated and is therefore particularly applicable to the coastal zone.

2.1 The Nesting Procedure

The nested model essentially consists of two separate models, the PG model and the CG model, which are coupled and synchronous. It uses an overlapping grid structure consisting of a single outermost

PG and one or more inner CGs. The grid structure allows multiple nesting so that any CG can become a parent to further children; in this way CGs may be telescoped to achieve any required spatial resolution. Any whole integer value may be used for the spatial nesting ratio r_s, that is, the ratio of the PG spacing to the CG spacing ($\Delta x_p/\Delta x_c$). The CG solutions may also be refined in time as well as space. The temporal nesting ratio r_t, the ratio of the PG timestep to the CG timestep ($\Delta t_p/\Delta t_c$), can be set to any integer value but is generally set to the same integer value as r_s. Figure 2 shows a schematic of the nested model.

The time integration of the model uses a 'bottom-up' approach. Before any PG can be integrated forward in time, all of its children must be integrated to the parent's current time-level. An overview of the procedure is shown in Figure 3. For simplicity, the time integration is only shown for two levels of nesting, the first at a 3:1 nesting ratio and the second at a 2:1 ratio. Since Δt_c is the CG timestep, Δt_{c1} and Δt_{c2} are the timesteps used by the CG at the first and second levels of nesting, respectively. Timesteps are numbered in the order of model progression. The procedure is described as follows:

1) the model integrates the outermost parent grid by a single timestep to time $t+\Delta t_p$
2) the model integrates all of the CGs at *nl=1* by a single timestep to time $t+\Delta t_{c1}$
3) the model integrates all of the CGs at *nl=2* up to the current time-level of their parent grids at *nl=1* ($t+\Delta t_{c1}$)
4) steps (2) and (3) are repeated until all child grids have been integrated to $t+\Delta t_p$
5) steps (1) through (4) are repeated

2.2 Reducing Boundary Errors

The model results of Section 3.1 illustrate the generation of boundary errors in a CG domain and distinguish between BFEs and BSEs. To reduce BFEs, waveforms leaving the PG must enter the CG without any distortion, while waves leaving the CG must pass through the boundary without and reflection (Garcia-Menendez and Odman (2011). Distortion of an incoming PG wave means mass and momentum are not conserved, thus, a conservative BC is required. Wave reflection, and subsequent generation of noise in the CG solution, can arise when the CG solution computed near the boundary interface is inconsistent with the PG data imposed along the CG boundary (Debreu and Blayo, 2008). The choice of boundary condition and the use of a ghost cell approach to formulation of the governing equations on the CG boundary were central to reducing BFEs in the present model. BSEs were reduced by careful placement of CG boundaries in areas of high PG accuracy. The details of the treatment of the CG boundary interface are explained in the following sections. Section 3 then presents model results which demonstrate the effectiveness of this approach.

2.2.1 The Boundary Condition

The BC implemented in the nested model consists of a Dirichlet boundary condition and a linear interpolation technique. The Dirichlet boundary condition directly imposes the PG solution ϕ_p on the CG solution ϕ_c along the CG boundary Γ, such that $\phi_c=\phi_p$. The Dirichlet condition can cause reflection of outgoing waves in nested models (Oddo and Pinnardi, 2008) when inconsistencies between the computed and imposed boundary data are significant. For this reason, relaxation and radiation BCs were also tested. The relaxation condition relaxes the CG solution towards the PG solution in an area (typically a few grid cells wide) known as the sponge layer. The sponge layer solution is calculated as $\phi_s = (1-\tau)\phi_c + \tau\phi_p$ where τ is a relaxation function which decreases from 0 on Γ (the inner boundary of the sponge layer), to 1 on the outer boundary of the sponge layer. The radiation condition is based on advective extrapolation and uses extrapolation to evacuate outgoing waves from CG to PG. The direction of flow at a boundary grid cell is first determined from the normal CG velocity component, $U_c\big|_{(i,j)}$. For outgoing flows $(U_c\big|_{(i,j)} > 0)$ the boundary velocity is calculated by linear extrapolation using two adjacent interior grid cells. For incoming flows $(U_c\big|_{(i,j)} > 0)$ the Dirichlet condition ($\phi_c=\phi_p$) was applied. Of the three BCs tested, the Dirichlet condition was found to achieve best results (see Section 3.2).

Due to the different spatial resolutions of PG and CG models, PG data must be interpolated in space to produce a complete series of CG boundary data. It is important that the interpolation technique preserves the PG waveforms, thereby conserving mass and momentum. A number of interpolation schemes (zeroth order, linear, quadratic and inverse distance-weighted) were tested for their conservation properties (see Nash and Hartnett (2010) for details). Linear interpolation was found to give the highest levels of conservation of PG mass and momentum fluxes (see Section 3.2) and was therefore implemented.

2.2.2 Ghost Cell Approach to Boundary Formulation

The finite difference formulae used to solve the governing continuity and momentum equations in a model require values from adjacent points on the grid which may be one, two or even three grid cells away. At an open boundary, application of these formulae then requires values which lie outside the grid and it becomes necessary to modify the formulae in such a way that they do not require external values. Such modification often involves simplification of the formulae, for example assuming linearity (in a non-linear model) in the momentum equations on the boundary or setting the horizontal viscosity to zero near the boundary (Herzfeld, 2009).

The present model uses the central differencing method to approximate the governing differential equations. Taking the example of the internal grid cell *(i,j)* in Figure 1, the finite difference approximation of the partial derivative of the flux component q_x in the x-direction is calculated at timestep *n* as:

$$\left.\frac{\partial q_x}{\partial x}\right|_{i+\frac{1}{2},j}^{n} = \frac{q_x\big|_{i+1,j}^{n} - q_x\big|_{i,j}^{n}}{\Delta x} \tag{1}$$

Since values for $q_x\big|_{i,j}^{n}$ and $q_x\big|_{i+1,j}^{n}$ are not specified on the space-staggered grid they must be calculated by linear interpolation using adjacent grid values as follows:

$$\left.\begin{aligned} q_x\big|_{i,j}^{n} &= \frac{q_x\big|_{i-\frac{1}{2},j}^{n} + q_x\big|_{i+\frac{1}{2},j}^{n}}{2} \\ q_x\big|_{i+1,j}^{n} &= \frac{q_x\big|_{i+\frac{1}{2},j}^{n} + q_x\big|_{i+1\frac{1}{2},j}^{n}}{2} \end{aligned}\right\} \tag{2}$$

The approximation of $(\partial q_x/\partial x)\big|_{i+\frac{1}{2},j}^{n}$ therefore requires the values of $q_x\big|^{n}$ at the adjacent grid points in the positive and negative x-direction. This requirement can be satisfied for an interior grid point; however, at an open boundary only the internal adjacent grid point exists. As a result, these partial derivatives cannot be calculated and are set to zero. In the context of the nested model, the formulation of the CG open boundaries in this manner meant the simplification of the advective acceleration and turbulent diffusion terms in the momentum equations. This was found to result in a loss of mass and, to an even greater extent, momentum at the CG boundary causing significant BFEs in the CG solution (see Section 3.2).

While BFEs arising from the choice of BC have long been recognised as important sources of error in nested models (see Koch and McQueen (1987)) BFEs arising from the formulation of the governing equations on nested boundaries as discussed here have not been studied in any great detail; however, results presented in Section 3.2 show that they can be significant. They were reduced through an original approach to the mathematical formulation of the nested boundary where ghost cells were introduced to the CG domain outside the CG boundaries. A schematic representation of this ghost cell approach is shown in Figure 4; for clarity CG variables are only shown for the boundary interface (shaded grey). The availability of the ghost cells prevents the need for simplification of the boundary formulations; thus boundary grid cells can use the same mathematical formulations of the governing equations as internal grid cells - in this way the CG boundary is said to be internalised.

Boundary data are interpolated from the PG and specified at both the ghost cells and the internal boundary cells. At ghost cells, only velocity and flux components normal to the boundary require specification while all variable values are specified at internal boundary cells. Taking the example of the boundary parallel to the J-axis in Figure 4, normal velocities and fluxes, U and q_x respectively, are specified along interface 'a' for the ghost cells and interface 'c' for the internal boundary cells. Water surface elevations, ζ, and tangential velocity and flux components, V and q_y respectively, are also specified along interface 'b' for the internal boundary cells. The internal boundary approach was found to ensure a high level of conservation of both mass and momentum at the CG boundary, thereby reducing boundary formulation errors and enabling the computation of highly accurate CG solutions.

2.2.3 Reducing Boundary Specification Errors

Due to lower resolutions, PG solutions will usually contain some level of inaccuracy compared to a higher resolution solution. BSEs are therefore an inherent problem in nested models as any inaccuracy in PG data specified at CG boundaries will propagate into the interior CG domain (Herzfeld, 2009). BSEs can be reduced by ensuring that CG boundaries are located in areas of high PG accuracy. In the present research, PG error was quantified by calculating the tidally-averaged relative error (RE_T) field, which is based on the relative error as defined by Thomann (1982).

RE_T is expressed as a percentage and quantifies the error in a PG solution relative to a reference solution. The reference solution is computed by a single grid (SG) model of the PG domain using the higher resolution of the proposed CG. The error in a PG hydrodynamic variable at a particular grid cell *(i,j)* is then calculated as:

$$RE_T(i,j) = \frac{\sum_{n=1}^{N} \left| \phi_p^n(i,j) - \phi_s^n(i,j) \right|}{\sum_{n=1}^{N} \left| \phi_p^n(i,j) \right|} \tag{3}$$

where $\phi_p^n(i,j)$ and $\phi_s^n(i,j)$ are the hydrodynamic variables calculated by the PG and SG models respectively at grid cell *(i,j)* and output time *n*, and *N* is the total number of output times during a tidal cycle. It was found that the smallest number of output times required to give an accurate measure of $RE_T(i,j)$ was 25; this corresponds to an output interval of 30 minutes for a typical tidal cycle of 12.5 hours. This finding is validated in Section 3.1. Current speeds were found to be a more accurate measure of PG error than water surface elevation as the latter remains relatively accurate regardless of the model resolution. RE_T in current speeds are plotted as a spatially-distributed error map. RE_T can also averaged across the model domain to give a single error value, RE_D - the domain-averaged

relative error. The tidally-averaged absolute error, AE_T, can also be useful to analyse in conjunction with RE_T and is computed as follows:

$$AE_T(i,j) = \sum_{n=1}^{N} \left| \phi_p^n(i,j) - \phi_s^n(i,j) \right| \Big/ N \qquad (4)$$

3 Testing of the Nesting Scheme

The idealised rectangular harbour model shown in Figure 5a was used to test the effectiveness of the nesting scheme with respect to the reduction of boundary errors. The accuracies of PG and CG solutions were determined by quantifying errors in these solutions relative to a SG reference solution. The determination of nested model accuracy in this way is a standard approach where an analytic solution of the test case does not exist (e.g. Spall and Holland (1991); Ginis et al. (1998); Blayo and Debreu (1999); Rowley and Ginis (1999)).

The Harbour measured 12km x 6km in plan, with bed depth decreasing from 10m at the sea boundary to 4m at the back of the harbour. A tide of constant period (12.5hrs) and range (3m) was simulated. A single CG was modelled at a 3:1 nesting ratio. Resolution details for the SG, PG and CG models are provided in Table 1. The harbour wall was included to induce non-rectilinear flows that were sensitive to model resolution.

3.1 PG Accuracy and Validation of RE_T

Figure 5b shows RE_T in PG current speeds calculated using equation (3). There was significant variation in error across the domain and the highest errors were recorded in the waters to either side of the harbour wall where non-rectilinear flows prevailed and at the back of the harbour. As stated, a value of N=25 was used to compute RE_T. By way of validation, RE_T was also calculated using timeseries data output at ten different locations spread throughout the extents of the PG domain (see Figure 5b). The timeseries data was output every six minutes giving N=125 for a 12.5hr tidal cycle. Table 2 compares the two sets of RE_T values. It can be seen that using N=25 instead of N=125 has a negligible effect on the magnitude of the computed error.

When computing RE_T, areas of low hydrodynamic activity can be problematic. In such areas, an absolute error of quite low magnitude small can represent a large relative error. For example, the large RE_T values at the back of the harbour in Figure 5b equate to tidally-averaged absolute errors of the order of 10^{-5} m/s and are therefore insignificant. An error filter was developed to remove insignificant errors from the RE_T field. To apply the filter, the average maximum current speed, U_{AM}, for the domain is first computed to determine the average level of hydrodynamic activity. A lower threshold absolute error, AE_T, is then calculated as 3% of the average maximum speed ($AE_T = 0.03U_{AM}$); any

AE_T value lower than this threshold is deemed to be insignificant and the corresponding RE_T value is set to zero as follows:

$$\text{If: } AE_T\big|_{i,j} \le AE_C \qquad \text{then: } RE_T\big|_{i,j} = 0 \qquad for\ i=1,2,3\ldots i_{max};\ j=1,2,3\ldots j_{max} \quad (5)$$

Figure 6 shows the RE_T in PG current speeds following application of the error filter. Comparing this with Figure 5b, it is seen that the significant errors either side of the harbour wall are preserved whilst the insignificant errors at the back wall are removed. The error filter is not applied to the rectangular harbour results presented in the following sections but it is applied to the results of the two test cases in Section 4.

3.2 Reducing BFEs

To evaluate the performance of the nesting scheme, it was necessary to distinguish BFEs from BSEs. This was done by using boundary data sourced from the high resolution SG model to eliminate BSEs. Any errors subsequently generated in the CG could only be BFEs. By way of demonstration, Figure 7a shows RE_T in CG current speeds when the boundary was formulated without ghost cells, using instead the simplified advective acceleration and turbulent diffusion terms. BFEs are highest near the boundary with RE_T values of greater than 5% but they dissipate with distance from the boundary. RE_D was 1.1% with standard deviation σ = 1.8%. By contrast, Figure 7b shows RE_T in CG current speeds when the boundary was formulated using ghost cells. With the exception of the errors at the back wall of the harbour, which represent insignificant differences in speed of the order of 10^{-5}m/s, CG errors were close to zero - RE_D was 0.08% with σ = 0.09%.

The reason for the reduction in BFEs was the improved conservation qualities of the ghost cell boundary formulation, particularly for those periods when flow was incoming from PG to CG. This is demonstrated by Figure 8a which compares momentum fluxes across the CG1 boundary interface computed by the SG model with those from the CG models with and without the ghost cell boundary formulation. Mass and momentum are seen to be fully conserved when the ghost cell formulation is employed. It was also found that in the absence of the ghost cell boundary formulation mass and momentum were not propagated correctly into the CG domain during periods of incoming flow. Figure 8b compares incoming SG and CG mass and momentum fluxes across the grid cells immediately inside and adjacent to the CG1 interface for the period of incoming flow. The CG flux computed using the ghost cells is seen to match the corresponding SG flux and, as would be expected, both are quite similar to the boundary fluxes in Figure 8a. In contrast, the CG flux computed without the ghost cells is significantly different to the SG flux. This is partly explained by the initial error in the boundary flux but the peak flux values are also substantially lower than the corresponding values

on the boundary (Figure 8a) indicating further loss of momentum. The ghost cell boundary formulation ensures both conservation of momentum at the boundary and conservation of momentum transport into the interior CG domain.

3.3 Reducing BSEs

To investigate BSEs, the CG1 boundary was forced with data from the PG model. Figure 9a shows RE_T in CG current speeds for this simulation for which RE_D was 4% (σ = 5.1%). Since the boundary scheme had been proven to eliminate BFEs, the errors shown are BSEs arising from the specific placement of CG1 in an area of low PG accuracy. Comparing Figure 9a with Figure 7a it is seen that BSEs can be quite significant relative to BFEs; the magnitude of both the RE_T near the boundary and the RE_D were higher for BSEs. In a similar manner to BFEs, BSEs are also seen to propagate into the interior CG domain and dissipate with distance from the boundary. Two important conclusions follow from this observation:

(1) CG boundaries should be placed sufficiently distant from an area of interest such that any BSEs generated will have dissipated before reaching the AOI

(2) there is potential, for reasons of computational efficiency, to choose a CG boundary location closer to the AOI but located in an area of lower PG accuracy than one further away from the AOI, if it can be determined that that the resulting BSEs will not adversely affect the area of interest

To demonstrate, if the domain inside CG1 of Figure 5b is assumed the AOI then, taking computational efficiency as the sole CG boundary selection criterion, CG1 is the most desirable choice of boundary. By comparison, taking PG accuracy (as measured by RE_T in PG current speeds) as the sole selection criterion, CG2 is more preferable to CG1 but results in a much larger, and more computationally expensive, CG domain. A third option is CG3 which is located closer to the AOI than CG2, giving a smaller CG domain, but is also sited in an area of low PG accuracy which will result in the generation of BSEs. However, it is also located some distance from the AOI such that some dissipation of BSEs would be expected. Comparing the RE_T in CG current speeds within the AOI for the three different CG simulations (Table 3) the optimum boundary location is shown to be CG3 as although BSEs are generated (Figure 9b), they do not adversely affect the AOI. RE_D for CG1 was 0.8%; this was significantly lower than the 4% for CG1 and comparable to the 0.6% for CG2 which was achieved at a greater computational cost.

3.4 Boundary Condition Tests

To investigate the effect of the BC on nested model performance, three nested models were developed using Dirchlet, relaxation and radiation boundary conditions. The models were otherwise identical, all used the ghost cell boundary formulation and all used PG data to drive CG1. RE_T and RE_D in CG current speeds were compared. Table 4 lists RE_D and standard deviations in RE_D for each model. The

Dirichlet BC resulted in the lowest RE_D and standard deviation and was therefore deemed most suitable.

To investigate the conserving properties of the different interpolation techniques, mass and momentum fluxes across the CG1 interface were calculated by the PG model and output at 5 minute intervals over the course of a tidal cycle. These were then compared with fluxes also calculated using PG data but which had been spatially-interpolated onto the CG. The error in the CG flux relative to PG flux was used as a measure of conservation. From Table 5, it is seen that linear interpolation resulted in the lowest errors in mass and momentum fluxes and was implemented accordingly.

4 Applications to Test Cases

To evaluate performance, the nested model was used to simulate two different study areas:

1) a physical model of a square harbour

2) a natural inlet, Galway Bay

In both cases, the numerical models were validated using measured data and the nesting functionality (i.e. achievement of improved accuracy and computational savings) was verified by comparing PG and CG accuracies and model runtimes. Assessing model performance is a difficult process and many different techniques can be used to measure performance; Bennett et al. (2013) provide a very useful discussion of the most common techniques. Here, we use residual methods which calculate the residual, or error, in a pair of values y_i and $\hat{y}_i$ for the same point in time or space, i, where y_i and $\hat{y}_i$ are either observed and modelled values, respectively, or values computed by two different models (e.g. the SG and CG models).

4.1 Test Case 1: the Physical Model

The nested model was used to simulate a physical model of an idealised square harbour at a 1:1 scaling ratio. As shown in Figure 10, the square harbour, made from fibreglass panels, was placed centrally in the working area of a tidal basin. The harbour measured 1m x 1m in plan (Figure 11a) with walls 0.4m high. The entrance wall was 1.75m from the baffle wall of the basin, through which tidal flow entered and exited, and contained a single centrally-located entrance, 0.2m wide. The mean water depth in the working area was set to 0.27m above the bed and the electronic weir controlling tidal flow simulated a simple sinusoidal tide of amplitude 0.05m and period 789s. The geometry and tidal specifications for the physical model were selected using the conventional Froude law scaling relationships (see Olbert (2006) for more detail) to correspond to typical conditions found in real coastal systems.

The SG and PG domains both covered the full extents of the working area of the tidal basin with their open boundaries located along the baffle wall. The single CG domain comprised a sub-domain of the

working area containing the AOI - the square harbour - at a 4:1 nesting ratio. All model specifications are listed in Table 6. The dimensions of the modelled domain were such that the Coriolis effect was omitted from the governing equations. The numerical models were each run for eight tidal cycles. In the case of the nested model, the PG was run on its own for the first four tidal cycles to ensure steady state conditions had been achieved, at which point the CG was then switched on and the model run for a further four tidal cycles. Modelled and measured data were compared for the eighth, and final, tidal cycle of the simulations.

Using a Nortek 10 MHz acoustic doppler velocimeter (range: ±3cm/s), current velocities were measured at 40 locations inside the square harbour on the four transect lines shown in Figure 11b. Measurements were taken at one second intervals for approximately eight tidal cycles with steady state conditions being reached after five tidal cycles. Depth-averaged velocities were required to allow comparison with the numerical model. Depth-averaged velocities can be obtained from a measured velocity profile using a number of methods. In this instance, the one-step method was used which takes the velocity measured at 0.6H (H being water depth) as the depth-averaged velocity. This method assumes a logarithmic velocity profile and gives reliable results in uniform cross-sections with no large irregularities (Julien, 1998).

4.1.1 Validation of Numerical Models

The flow pattern in the square harbour is an example of tidally-pumped circulation. The flood tide (Figure 12a) enters the harbour through the constricted entrance as a confined jet while outward flow on the ebb tide (Figure 12b) is drawn from all around the entrance. The numerical models reproduced this circulation pattern, but to differing degrees of accuracy. Computed velocities were compared with measured velocities along the four transects of Figure 11b at the times of high water, mid-ebb, low water and mid-flood. Due to space limitations, graphical comparisons are only presented for Transect A at low water and mid-flood (Figure 13) but Table 7 compares root mean square errors in velocities along Transects A, B and C for all stages of the tide. As was expected, the higher resolution of the SG model meant it exhibited closer correlation with the measured data (i.e. lower RMSEs) than the PG model. This is particularly evident at the centres of the transects in Figure 13. Although, CG accuracy is discussed in more detail in the following sections, both Figure 13 and Table 7 show that the CG was more accurate than the PG and of a very similar accuracy to the SG.

4.1.2 Determination of PG Accuracy and Placement of CG Boundaries

PG accuracy was determined by calculating RE_T in PG water elevations and current speeds relative to SG values The PG water elevations were relatively accurate; RE_D for the full model domain was 1.8% which equated to an average absolute error of 1.2 mm per grid cell over a tidal cycle. In contrast, PG current velocities contained substantial errors (Figure 14). Error statistics for PG current speeds are

summarised in Table 8. RE_D in PG current speed was 16% and RE_T = 5% was exceeded in three-quarters (71%) of the domain. These errors are directly attributable to the lower resolution of the PG since they were highest in the waters within, and surrounding, the square harbour where spatial resolution was most influential. For the AOI (the square harbour) on its own, RE_D was 42.1% and RE_T = 5% was exceeded at all grid cells.

The CG boundaries, five in total, are shown in Figure 14. The locations were selected as follows. Based on RE_T in PG current speeds, potential boundaries were identified in areas of high PG accuracy, far enough away from the AOI that boundary errors would not adversely affect it, but close enough that the size of the CG domain and the associated computational effort were minimised. PG accuracy at potential boundary locations was further assessed by analysis of the mass and momentum fluxes across the proposed boundary interfaces. Figure 15a compares PG and SG momentum fluxes across the B1 boundary interface. The average error in PG values over a tidal cycle was less than 3%; PG data was therefore highly accurate along this boundary. Similar levels of accuracy were in evidence at the other CG boundaries.

4.1.3 Determination of CG Accuracy

Figure 16 compares RE_T in CG current speeds (in the AOI only) with those from the PG model. The CG is clearly more accurate than the PG. Table 8 shows that RE_D in current speed dropped from 42.1% for the PG to 0.7% for the CG. CG accuracy was further verified by comparison of SG, PG and CG current speed timeseries at various locations in the AOI. Figure 17 shows two such comparisons for the period of a full tidal cycle. The low accuracy of the PG (relative to the SG) is clearly apparent, as is the high accuracy of the CG; for much of the time CG and SG data points are coincident. The improvement in accuracy can be quantified by comparing mean errors in the time series. At Point A, where the mean current speed was 1.67 m/s, PG mean error was 0.95 m/s (σ = 0.59 m/s) while CG mean error was significantly lower at 0.04 m/s (σ = 0.03 m/s). Similarly, at Point B where mean current speed was 0.92 m/s, PG mean error was 0.17 m/s (σ = 0.16 m/s) and CG mean error was just 0.02 m/s (σ = 0.01 m/s).

4.1.4 Effect of Boundary Placement on CG Accuracy

In the absence of an informed CG boundary selection procedure, B1' in Figure 14 might appear a feasible alternative to B1, from the point of view of minimising CG size and, thus, computational cost. However, RE_T in PG current speeds showed that the PG solution was quite inaccurate along B1' and subsequent analysis of PG and SG momentum fluxes across the B1' interface (Figure 15b) revealed a mean error of 22% in PG momentum flux over a tidal cycle. This represents a substantial deterioration in PG accuracy from the B1 interface (3% mean error). If B1' were used in place of B1

one would then expect a significant increase in BSEs in the CG solution; this was indeed the case as demonstrated by Figure 16c which shows RE_T in CG current speeds for this scenario. A comparison with Figure 16b shows a significant deterioration in CG accuracy and highlights the importance of boundary location for nested model accuracy.

4.2 Test Case 2: Galway Bay

Galway Bay (Figure 18) is a large macro-tidal bay on the west coast of Ireland. It can be divided into two sections, the inner bay and the outer bay. The inner bay is relatively shallow with depths less than 30m below spring high water. The outer bay extends seaward to the Aran Islands, gradually deepening to approximately 60m in the passages to the northwest and southeast of the islands where it meets the Atlantic Ocean. Tidal range varies from 4.5m on spring tides to 1.9m on neap tides. The main freshwater inflow is the River Corrib with a mean annual flow of $2.96 \times 10^9 m^3$.

The PG and SG model domains covered the full extents of the domain shown in Figure 18, an area measuring approximately 57 x 33 km^2. A single CG, at a 3:1 nesting ratio, was used to model the inner bay. Two CG boundaries were specified. The western boundary ran from Spiddal on the northern coast of the bay, to Blackhead on the southern coast, and the northern boundary spanned the River Corrib. The PG used a spatial resolution of 300m while the CG was resolved at 100m. The model parameters are summarised in Table 9.

4.2.1 Validation of Numerical Models

Figure 19a compares SG modelled current speeds with measured current speeds at GB1 (see Figure 18) which is located on the western CG boundary near the northern shore. Figure 19b compares SG modelled water surface elevations with measured water levels at GB2, located inside the AOI. The SG model demonstrated acceptable agreement with the measured data. The mean absolute errors in current speeds and water surface elevations were 0.023 m/s (σ = 0.018 m/s) and 0.145 m (σ = 0.089 m), respectively.

The superior accuracy of the SG model over the PG model is demonstrated in Figure 20 which compares modelled spring tide current speeds with measured ADCP data at GB3 in the outer bay (see Figure 18). SG values show noticeably better correlation with measured data than PG values. Comparing mean absolute errors in these data, SG error was almost half the PG error; mean PG error was 0.064 m/s (σ = 0.046 m/s) and mean SG error was 0.036 m/s (σ = 0.026 m/s). The high level of agreement between SG and measured values at both GB1 and GB3, and the higher accuracy of SG relative to PG at GB3 justifies the use of the SG model as the reference solution.

4.2.2 Accuracy of PG Solution

Figure 21 shows RE_T in PG water elevations and current speeds. Errors are only presented for the AOI (see Figure 18 for extents). The inaccuracy of the PG solution is clearly visible from the RE_T plots. As expected, the inaccuracies were highest in shallow water areas where the more complex topography required a higher resolution. While the errors in water elevations were relatively low, 1% RE_T was still exceeded in 20% of the AOI. The areas of greatest errors in elevation corresponded to the intertidal areas which were subject to flooding and drying. Errors in current speeds were significantly higher than those in surface elevations; RE_T in current speed of 5% was exceeded in 44% of the AOI and RE_D in current speed was substantial at 13.4%.

4.2.3 Accuracy of CG Solution

RE_T in CG water surface elevations and current speeds are presented in Figure 22. For consistency, errors are again only displayed for the AOI. Significant improvements in accuracy over the PG solution can be observed for both elevations and current speeds.

Looking first at surface elevations (Figure 22a), RE_T = 1% was exceeded in less than 1% of the AOI compared with 20% for the PG. The improved accuracy of the CG is particularly noticeable in inter-tidal areas. The only area within which 1% RE_T was exceeded was the Corrib river channel. From Figure 21, it is seen that the PG solution contained significant errors at the point where the CG boundary was located in the Corrib channel. Although this was known in advance, there was no suitable alternative location for the northern boundary. The CG errors observed in the channel are a direct result of the specification of inaccurate boundary data from the PG model and are, therefore, BSEs. As previously shown, boundary errors will propagate into the interior domain, but will usually dissipate within a relatively short distance of the CG boundary. In this instance, the narrow width of the river channel meant the boundary errors propagated further into the domain than is typical. The level of CG error in the channel was commensurate with the level of PG error present at the CG boundary, which at RE_T = 3% was relatively low in any case. With the exception of the Corrib channel, CG surface elevations were almost identical to SG elevations and RE_D in CG elevations was just 0.16%.

Looking next at current speeds (Figure 22b), the improvement in CG accuracy was equally as significant as that for water surface elevations. The proportion of the AOI within which RE_T = 5% was exceeded fell from 44% in the PG to 3% in the CG; RE_D dropped accordingly from 13.4% to 0.4%. The BSEs in surface elevations in the Corrib channel were also present in the current speeds and, again, the level of CG error in the channel (RE_T = 12%) was similar to the level of PG error (RE_T = 8%).

The improvement in accuracy from PG to CG was also observed in time series comparisons. Figure 23 compares current speeds computed by the SG, PG and CG models at two locations in the AOI, Site 2 and Site 4 (see Figure 18 for locations). PG speeds are visibly different in magnitude to SG speeds and there is also a noticeable phase difference, particularly at Site 2. In contrast, CG speeds closely match SG speeds and there is no phase difference between the two curves. Mean absolute errors in the PG data shown (relative to the SG data) were 0.036 m/s (σ = 0.021 m/s) for Site 2 and 0.015 m/s (σ = 0.011 m/s) for Site 4. By comparison, the mean errors in CG data were an order of magnitude lower: 0.003 m/s (σ = 0.002 m/s) at Site 2 and 0.001 m/s (σ = 0.0010 m/s) at Site 4.

4.3 Computational Savings

The purpose of a nested model is to reduce the computational cost of high resolution modelling through the use of selective mesh refinement. The nested model must therefore not only produce equivalent accuracy to a high resolution single grid model but must do so at a lower computational cost. The former has been verified; to verify the latter, run-times of the SG and nested models were recorded and compared for the two test cases and for the idealised rectangular harbour (Table 10). All model simulations were conducted on a Lenovo Thinkstation E20 with 3.06GHz Intel Xeon processor and 8GB RAM. It is seen that significant computational savings were achieved for the two test cases - 72% for Test Case 1 and 66% for Test Case 2. Run-times for numerical models are largely governed by the number of computations which must be completed. Treating all calculations at a particular grid cell and timestep as a single computation, the total number of computations for a simulation is the number of grid cells by the number of simulation timesteps (these are also listed in Table 10). For the present research, the nested model run-time, NM_t, can therefore be estimated by summing the time required to complete all computations on the PG and the CG, as follows:

$$NM_t = PG_t + \frac{CG_{cells}}{SG_{cells}} SG_t \tag{6}$$

where PG_t and SG_t are the PG and SG model run-times, and CG_{cells} and SG_{cells} are the number of grid cells in the CG and SG domains. It follows that the computational saving, CS, achieved by the nested model relative to the SG model can be estimated as:

$$CS = \left[1 - \frac{CG_{cells}}{SG_{cells}} - \frac{PG_{time}}{SG_{time}} \right] \tag{7}$$

By switching off a flag in the nested model, the CG code is bypassed and the PG model runs alone. PG model run-times were recorded in this way and estimates of nested model computational savings

were computed using equation (7). Comparison of estimated savings with recorded savings in Table 10 shows there is good correlation between the two; however, the estimated savings are consistently higher due to the omission from equation (7) of the additional run-time required for read-write operations and specification of the CG boundary data. Given the difference between the estimated and recorded savings is only 5% on average, it can be concluded that the equation does give a useful indication of the likely computation savings for a particular nested model application.

5 Summary and Conclusions

A one-way nested model for the simulation of tidal hydraulics has been developed with particular applications to down-scaling in coastal waters. Boundary errors can be a significant source of errors in one-way nested models. Boundary formulation errors occur when the boundary condition and/or formulation of the governing equations on the boundary lead to poor conservation of mass and momentum at the child grid boundary when flows are incoming from parent to child and reflection of waveforms at the child grid boundary when flows are incoming from child to parent. Boundary specification errors occur where child grid boundaries placed in unsuitable locations result in the specification of inaccurate boundary data to the child grid domain. The main focus of this research was the development and testing of a nesting scheme designed to reduce the generation of boundary errors. The important elements of the nesting scheme include:

- the use of a boundary condition and interpolation procedure which conserves mass and momentum when parent grid data is passed to the child grid at the child grid boundary
- a ghost-cell approach to boundary formulation which helps momentum conservation
- a procedure for identifying suitable child grid boundary locations so that parent grid errors are not passed to the child via the child grid boundary

The main conclusions based on this research can be summarised as follows:

- by incorporating values from ghost cells outside the domain, governing equations can be formulated at child boundary grid cells in a manner similar to interior grid cells. This internal boundary approach to formulation of nested boundaries improves the transition of mass and momentum across the boundary interface thereby ensuring high levels of conservation and low boundary formulation errors
- careful placement of child grid boundaries is crucial to the attainable accuracy of a child grid solution. Boundaries must be placed in areas of high parent grid accuracy to minimise boundary specification errors, and at sufficient distances from the area of interest so that boundary errors do not adversely affect model performance in the area of interest. RE_T in parent grid current speeds provides a very useful tool for identification of areas of high parent grid accuracy which are suitable for location of child grid boundaries.

- the nested model was tested for both experimental and natural environments. In both cases, the child grid solutions were found to demonstrate significant improvements in accuracy over the lower resolution parent grid solutions. They also demonstrated similar levels of accuracy to high resolution, single grid models for a much lower computational cost. A computational saving of 72% was achieved for the square harbour model while 66% was achieved for Galway Bay.
- the nested model is extremely robust; it performs equally well for child grids with single or multiple open boundaries, for shallow inter-tidal waters or deeper coastal waters and for experimental or natural environments
- the nesting scheme presented is quite generic and could be easily implemented in any oceanographic, or indeed atmospheric, model where down-scaling is desired and where boundary data are available from a larger-scale model.
- in the event that the nesting scheme were employed in another modelling system, the simple formula presented for computational savings (equation (7)) provides a reasonably accurate estimate of the computational savings that would be achieved. The equation could also prove useful when making decisions on child grid boundary locations as run-time is directly proportional to the size of the child grid.

Note: the nested model code is available, free of charge, to academic researchers upon request from the authors.

References

Barth A, Alvera-Azcarate A, Rixen M and Beckers J-M (2005) Two-way nested model of mesoscale circulation features in the Ligurian Sea. *Progress in Oceanography* 66: 171–189.

Baumhefner DP and Perkey DJ (1982) Evaluation of lateral boundary errors in a limited domain model. In: Koch SE and McQueen JT (1987) *A survey of nested grid techniques and their potential for use within the MASS weather prediction model*. NASA Technical Memorandum 87808, National Aeronautics and Space Administration, USA.

Bennett ND, Croke BFW, Guariso G, Guillaume JHA, Hamilton SH, Jakeman AJ, Marsili-Libelli S, Newham LTH, Norton JP, Perrin C, Pierce SA, Robson B, Seppelt R, Voinov AA, Fath BD and Andreassian V (2013) Characterising performance of environmental models. Environmental Modelling & Software 40: 1-20.

Blayo E and Debreu L (1999) Adaptive mesh refinement for finite-difference ocean models: First experiments. *Journal of Physical Oceanography* 29: 1239-1250.

Blayo E and Debreu L (2005) Revisiting open boundary conditions from the point of view of characteristic variables. *Ocean Modelling* 9: 231-252.

Cailleau S, Fedorenko V, Barnier B, Blayo E and Debreu L (2008) Comparison of different numerical methods used to handle the open boundary of a regional ocean circulation model of the Bay of Biscay. *Ocean Modelling* 25: 1-16.

Debreu L and Blayo E (2008) Two-way embedding algorithms: a review. *Ocean Dynamics* 58: 415-428.

Debreu L, Marchesiello P, Penven P and Cambon G (2012) Two-way nesting in split-explicit ocean models: Algorithms, implementation and validation. *Ocean Modelling* 49-50: 1-21.

Deleersnijder E and Lermusiaux PFJ (2008) Multi-scale modeling: nested-grid and unstructured-mesh approaches. *Ocean Dynamics* 58: 335–336

Falconer RA (1984) A mathematical model study of the flushing characteristics of a shallow tidal bay. *Proceedings of the Institution of Civil Engineers, Part 2, Research and Theory* 77(3): 311-332.

Falconer RA and Chen YP (1991) An improved representation of flooding and drying and wind stress effects in a 2-D tidal numerical model. P*roceedings of Institution of Civil Engineers, Part 2, Research and Theory* 91: 659-678.

Garcia-Menendez F and Odman MT (2011) Adaptive grid use in air quality modeling. *Atmosphere* 2: 484-509.

Ginis I, Richardson RA and Rothstein LM (1998) Design of a multiply nested primitive equation ocean model. *Monthly Weather Review* 126: 1054-1079.

Hartnett M, Nash S and Olbert I (2012) An integrated approach to trophic assessment of coastal waters incorporating measurement, modelling and water quality classification. Estuarine, Coastal and Shelf Science 112: 126-138, doi:10.1016/j.ecss.2011.08.012.

Hasegawa D, Sheng J, Greenberg DA and Thompson KR (2011) Far-field effects of tidal energy extraction in the Minas Passage on tidal circulation in the Bay of Fundy and Gulf of Maine using a nested-grid coastal circulation model. *Ocean Dynamics* 61:1845-1868

Hertzfeld M (2009) The role of numerical implementation on open boundary behaviour in limited area ocean models. Ocean Modelling 27: 18–32.

Herzfeld M and Andrewartha JR (2012) A simple, stable and accurate Dirichlet open boundary condition for ocean model downscaling. *Ocean Modelling* 43-44: 1-21.

Holt J, Harle K, Proctor R, Michel S, Ashworth M, Batstone C, Allen I, Holmes R, Smyth T, Haines K, Bretherton D and Smith G (2009) Modelling the global coastal ocean. *Philosophical Transactions of the Royal Society A* 367: 939-951.

Janekovic I and Powell B (2011) Analysis of imposing tidal dynamics to nested numerical models. *Continental Shelf Research* 34: 30-40.

Julien PY (1998) *Erosion and sedimentation*. Cambridge University Press, Cambridge, UK.

Koch SE and McQueen JT (1987) *A survey of nested grid techniques and their potential for use within the MASS weather prediction model*. NASA Technical Memorandum 87808, National Aeronautics and Space Administration, USA.

Korres G and Lascaratos A (2003) A one-way nested eddy resolving model of the Aegean and Levantine basins: implementation and climatological runs. *Annales Geophysicae* 21: 205–220.

Lavelle JW and Thacker WC (2008) A pretty good sponge: dealing with open boundaries in limited-area ocean models. *Ocean Modelling* 20: 270-292.

Leitão P, Coelho H, Santosa A and Nevesa R (2005) Modelling the main features of the Algarve coastal circulation during July 2004: a downscaling approach. *Journal of Atmospheric & Ocean Science* 10(4): 421-462.

Marchesiello P, McWilliams J and Shchepetkin A (2001). Open boundary conditions for long-term integration of regional oceanic models. *Ocean Modelling* 3: 1–20.

Mason E, Molemaker J, Shchepetkin AF, Colas F, McWilliams JC and Sangrà P (2010) Procedures for offline grid nesting in regional ocean models. *Ocean Modelling* 35: 1-15.

Nash S, Hartnett M and Dabrowski T (2010) Modelling phytoplankton dynamics in a complex estuarine system. Proceedings of the ICE - Water Management 164(1): 35-54, doi: 10.1680/wama.800087.

Nash S and Hartnett M (2010) Nested circulation modelling of inter-tidal zones: details of a nesting approach incorporating moving boundaries. *Ocean Dynamics* 60: 1479-1495.

Natural Environment Research Council (2009) E-science: Global coastal ocean modelling, url: http://www.nerc.ac.uk/research/programmes/escience/results/ocean.asp, accessed: 10/6/2009.

Oddo P and Pinardi N (2008) Lateral open boundary conditions for nested limited area models: a scale selective approach. *Ocean Modelling* 20: 134-156.

Olbert A (2006) *Investigations into turbulence processes in tide-induced flows: scale and numerical modelling*. PhD Thesis, Department of Civil Engineering, National University of Ireland Galway.

Olbert AI, Dabrowski T, Nash S and Hartnett M (2012) Regional modelling of the 21st century climate changes in the Irish Sea. *Continental Shelf Research* 41: 48-60.

Palma ED and Matano RP (1998) On the implementation of passive open boundary conditions for a general circulation model: The barotropic mode. *J. Geophys. Res.* 103 (C1), 1319–1341.

Rowley C and Ginis I (1999) Implementation of a mesh movement scheme in a multiply nested ocean model and its application to air–sea interaction studies. *Monthly Weather Review* 127: 1879-1896.

Ji X, Sheng J, Tang L, Liu D and Yang X (2011) Process study of circulation in the Pearl River Estuary and adjacent coastal waters in the wet season using a triply-nested circulation model. *Ocean Modelling* 38: 138-160.

Shan S, Sheng J, Thompson KR and Greenberg DA (2011) Simulating the three-dimensional circulation and hydrography of Halifax Harbour using a multi-nested coastal ocean circulation model. *Ocean Dynamics* 61(7): 951-976.

Spall MA and Holland WR (1991) A nested primitive equation model for oceanic applications. *Journal of Physical Oceanography* 21: 205-220.

Spall MA and Robinson AR (1989) A new hybrid coordinate open ocean primitive equation model. *Mathematics and Computers in Simulation* 31: 241-269.

Staneva J, Stanev EV, Wolff JO, Badewien TH, Reuter R, Flemming B, Bartholoma A and Boldinge K (2009) Hydrodynamics and sediment dynamics in the German Bight: A focus on observations and numerical modelling in the East Frisian Wadden Sea. *Continental Shelf Research* 29: 302-319.

Thomann RV (1982) Verification of water quality models. *Journal of Environmental Engineering* 108(5): 923-940.

Wang D-P (2012) Diurnal modulation of semidiurnal internal tides in Luzon Strait. *Ocean Modelling* 59-60: 1-10.

Wang X, Chao Y, Zhang H, Farrara J, Li Z, Jin X, Park K, Colas F, McWilliams JC, Paternostro C, Shum CK, Yi Y, Schoch C and Olsson P (2012) Modeling tides and their influence on the circulation in Prince William Sound, Alaska. *Continental Shelf Research*, http://dx.doi.org/10.1016/j.csr.2012.08.016

You SH, Lee W-J and Moon KS (2010) Comparison of storm surge/tide predictions between a 2-D operational forecast system, the regional tide/storm surge model (RTSM), and the 3-D regional ocean modeling system (ROMS). *Ocean Dynamics* 60: 443-459.

Zhang W-Z, Hong H-S, Shanga S-P, Chen D-W and Chaic F (2007) A two-way nested coupled tide-surge model for the Taiwan Strait. *Continental Shelf Research* 27: 1548-1567.

Tables

Physical Parameter	**SG**	**Nested Model**	
		PG	**CG**
L_X: - full domain - AOI	12 km	12 km	6 km
L_Y: - full domain - AOI	6 km	6 km	6 km
Tidal Amplitude:	1.5 m	1.5 m	1.5 m
Tidal Period	12.5 hrs	12.5 hrs	12.5 hrs
Resolution: - grid spacing - timestep	40 m 40 s	120 m 120 s	40 m 40 s
No. of grid cells	45,000	5,000	22,500
Bed Roughness	30 mm	30 mm	30 mm

Table 1: Specifications for idealised rectangular harbour models.

Location	RE_T **- Timeseries (n = 125)**	RE_T **- Snapshots (n = 25)**	**Difference**
1	7.50 %	7.51 %	0.01 %
2	7.90 %	7.91 %	0.01 %
3	14.33 %	14.48 %	0.15 %
4	21.28 %	21.89 %	0.61 %
5	20.99 %	21.82 %	0.83 %
6	8.80 %	8.85 %	0.05 %
7	14.80 %	14.76 %	-0.04 %
8	16.61 %	16.57 %	-0.04 %
9	6.97 %	6.71 %	-0.26 %
10	2.66 %	2.57 %	-0.09 %

Table 2: Comparison of RE_T in PG current speeds calculated using time series data and snapshot data. Locations 1-10 are shown in Figure 5b.

CG Boundary	RE_D	σ **in** RE_D
CG1	4.0 %	5.1 %
CG2	0.5 %	0.6 %
CG3	0.6 %	0.8%

Table 3: Comparison of CG error in AOI for three different CG boundaries (locations of AOI and CG boundary locations are shown in Figure 5b).

BC Type	RE_D	σ **in** RE_D
Dirichlet	4.0 %	5.1 %
Relaxation	5.6 %	7.4 %
Radiation	4.5 %	6.8%

Table 4: Comparison of CG error for three different BCs.

Interpolation Scheme	Tidal-averaged Error in CG Flux	
	Mass	Momentum
Zeroth-order	0.7 %	4.5 %
Linear	0.4 %	0.3 %
Quadratic	0.4 %	0.5 %
Inverse distance-weighted	0.7 %	4.7 %

Table 5: Comparison of tidal-averaged error in CG boundary mass and momentum fluxes calculated using spatially-interpolated PG data relative to those calculated by the PG model.

Physical Parameter	SG	Nested Model		Physical Model
		PG	CG	
L_X: - full domain	4.75 m	4.75 m	2.25 m	4.75 m
- AOI (square harbour)	1.00 m	1.00 m	1.00 m	1.00 m
L_Y: - full domain	5.0 m	5.0 m	2.5 m	5.0 m
- AOI (square harbour)	1.0 m	1.0 m	1.0 m	1.0 m
Mean Depth	0.27 m	0.27 m	0.27 m	0.27 m
Tidal Amplitude	0.05 m	0.05 m	0.05 m	0.05 m
Tidal Period	789 s	789 s	789 s	789 s
Resolution: - grid spacing	0.025 m	0.10 m	0.025 m	--
- timestep	0.05 s	0.20 s	0.05 s	--
No. of grid cells	38,000	2,400	9,000	--
Bed Roughness *	0.8 mm	0.8 mm	0.8 mm	0.8 mm

Table 6: Specifications for square harbour models [* the bed roughness coefficient was determined for the physical model using measured velocity profiles].

Transect	Stage of Tide	RMSE in x-direction velocity [mm/s]		
		SG	PG	CG
A	Mid-flood	1.18	1.46	1.22
	High water	0.65	0.67	0.66
	Mid-ebb	0.51	0.59	0.51
	Low water	0.46	0.62	0.48
B	Mid-flood	2.08	2.25	2.11
	High water	0.74	0.83	0.74
	Mid-ebb	0.63	0.67	0.65
	Low water	1.00	1.03	1.00
C	Mid-flood	1.66	1.81	1.68
	High water	1.26	1.40	1.28
	Mid-ebb	0.58	0.63	0.60
	Low water	0.37	0.40	0.37

Table 7: Comparison of root mean square errors between modelled and measured data.

Model Solution	Errors Statistics for RE_T in Current Speeds			
	RE_D	σin RE_D	% of domain where RE_T >5%	% of domain where RE_T >1%
PG: full domain	16.0 %	15.1 %	71.0 %	96.4 %
PG: AOI	42.1 %	15.7 %	100.0 %	100.0 %
CG: AOI	0.7 %	1.4%	0.0 %	22.8 %

Table 8: Summary of statistics for errors in PG and CG current speeds.

Physical Parameter	SG	Nested Model	
		PG	CG
L_X: - full domain - AOI	57 km	57 km	25.5 km
L_Y: - full domain - AOI	33.3 km	33.3 km	19.8 km
Tidal Amplitude: - spring - neap	2.5 m 1.0 m	2.5 m 1.0 m	2.5 m 1.0 m
Tidal Period	12.5 hrs	12.5 hrs	12.5 hrs
Resolution: - grid spacing - timestep	100 m 20 s	300 m 60 s	100 m 20 s
No. of grid cells	189,810	21,090	50,490
Bed Roughness	200 mm	200 mm	200 mm

Table 9: Specifications for Galway Bay models.

Model	Timesteps	No. of Grid Cells	Simulation Time [mins]	Computational Savings	Estimated Savings
Rectangular Harbour:					
SG	4,500	45,000	5.983	---	---
PG	1,500	5,000	0.267	---	---
NM (CG1)	4,500	22,500	3.450	42%	46%
NM (CG2)	4,500	36,000	5.333	11%	16%
NM (CG3)	4,500	29,250	4.417	26%	31%
Square Harbour:					
SG	63,360	38,400	79.167	---	
PG	15,840	2,400	1.230	---	
NM	63,360	8,400	22.183	72%	77%
Galway Bay:					
SG	4,500	189,810	16.583	---	---
PG	1,500	21,090	0.617	---	---
NM	4,500	50,490	5.567	66%	70%

Table 10: Computational savings achieved by the nested model (NM = nested model).

Figures

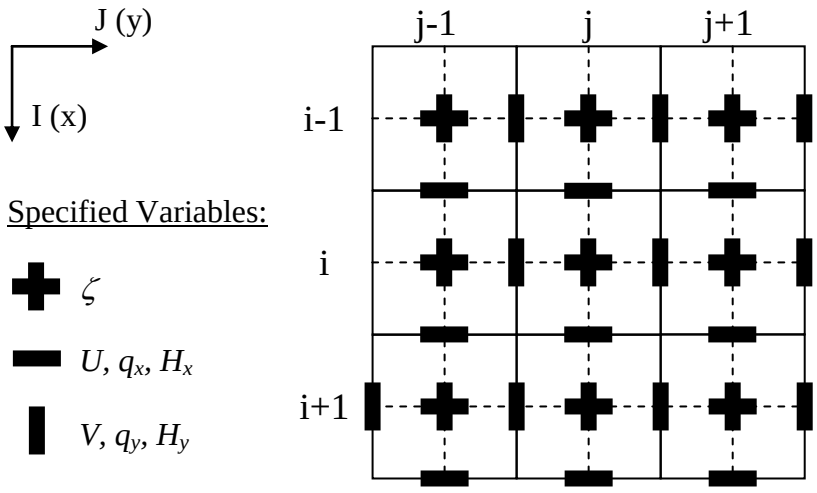

Figure 1: The space-staggered grid scheme and (*I*,*J*) coordinate system.

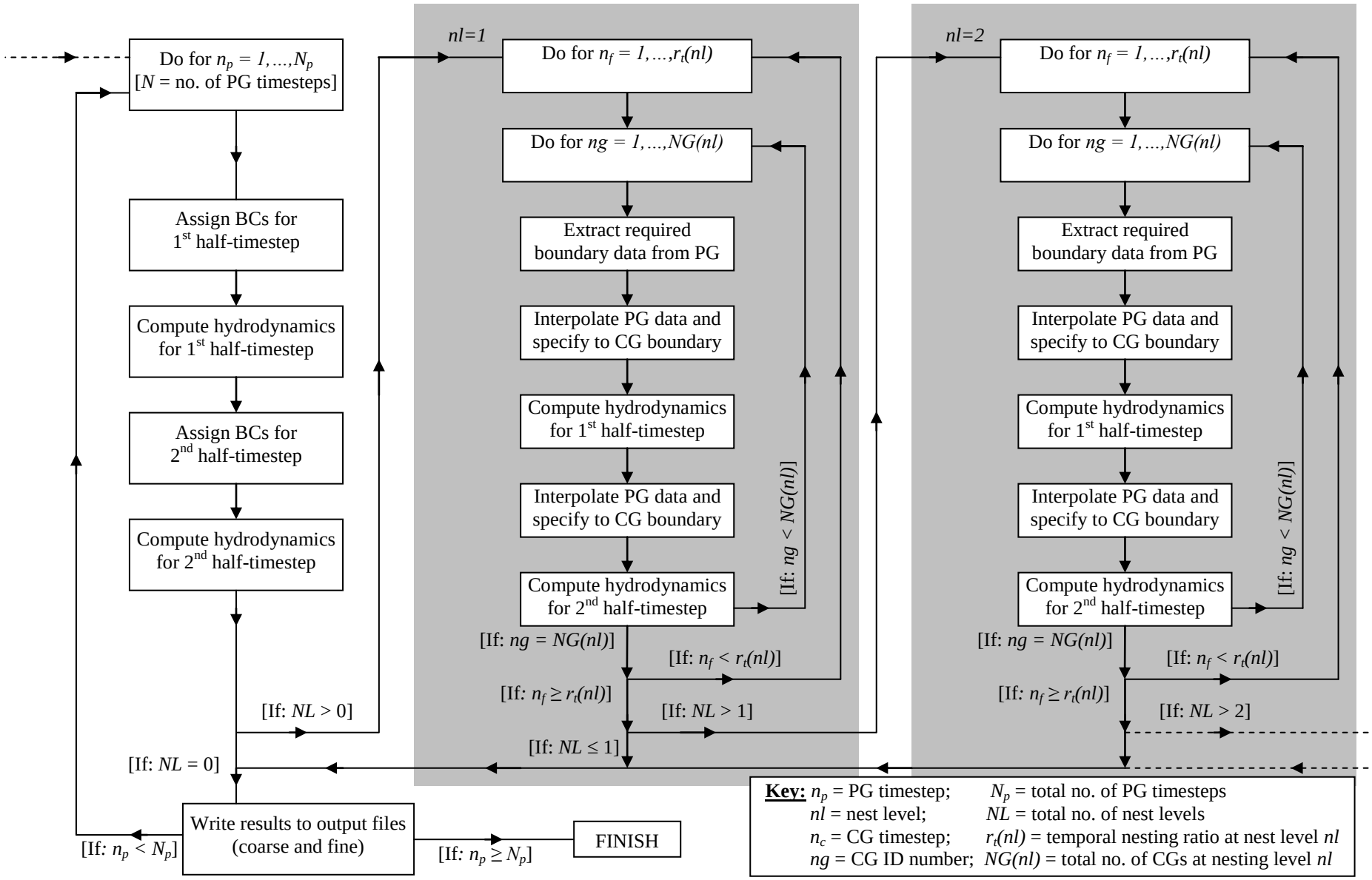

Figure 2: Schematic of nested model for single level of nesting (*NL*=1); non-shaded section is PG model, shaded section is CG model (data input and initialisation omitted).

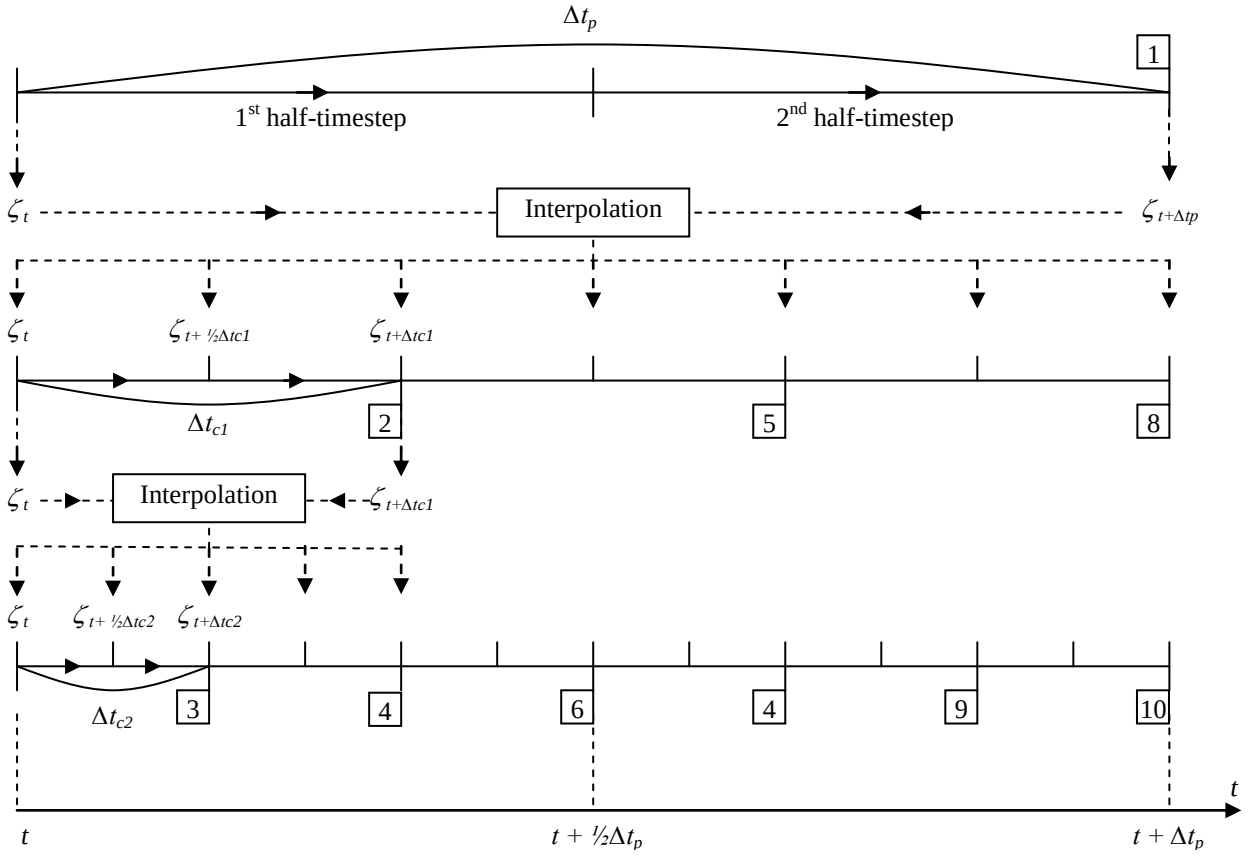

Figure 3: Time integration of the nested model for two levels of nesting, i.e. NL=2.

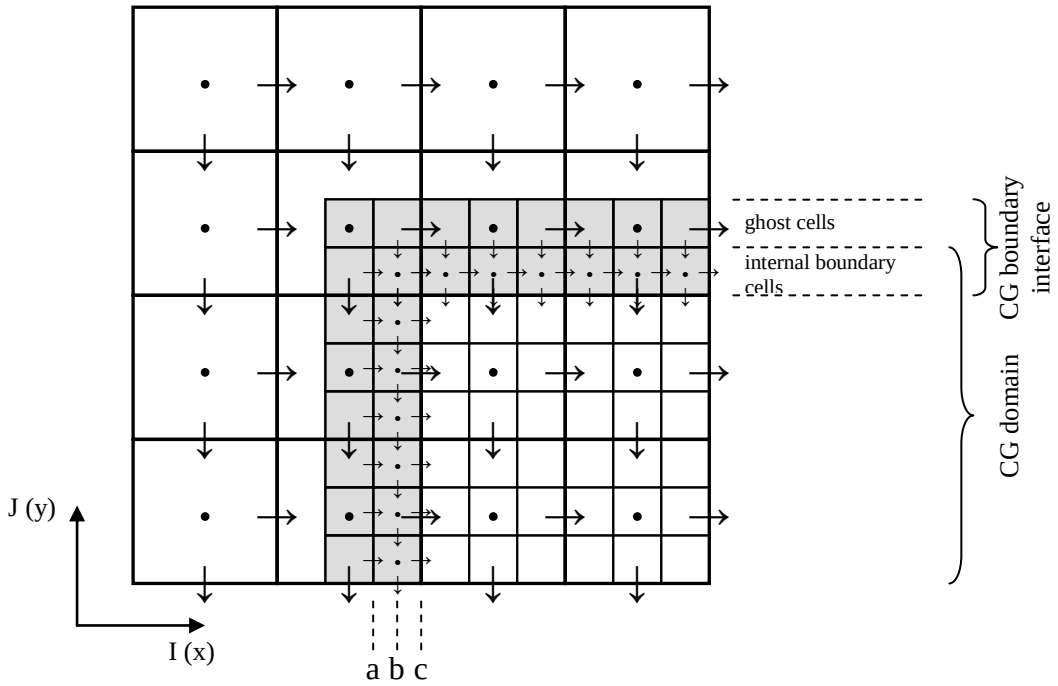

Figure 4: Schematic of the internal boundary configuration for a 3:1 nesting ratio.

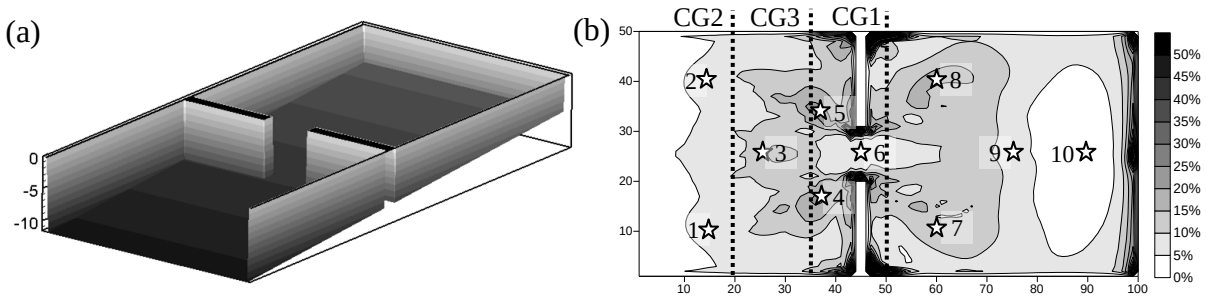

Figure 5: (a) Extents of rectangular harbour model domain and (b) RE_T in PG solution. Dotted lines indicate CG boundaries and stars denote time series locations. The AOI is the area to the right of CG1.

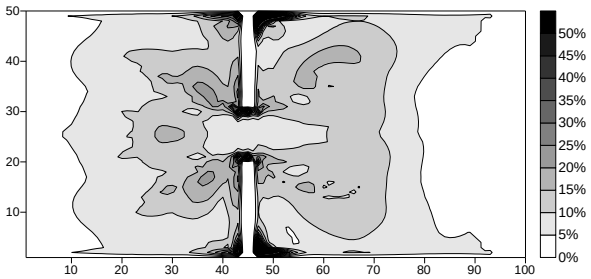

Figure 6: RE_T in PG current speed following application of the error filter.

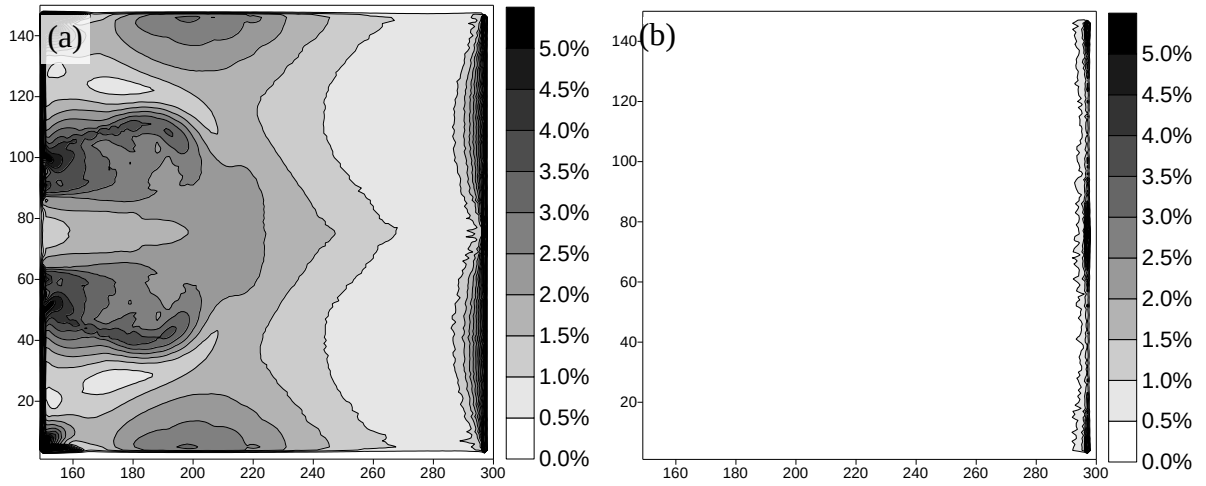

Figure 7: RE_T in CG forced with SG boundary data when boundary is formulated (a) without ghost cells and (b) with ghost cells.

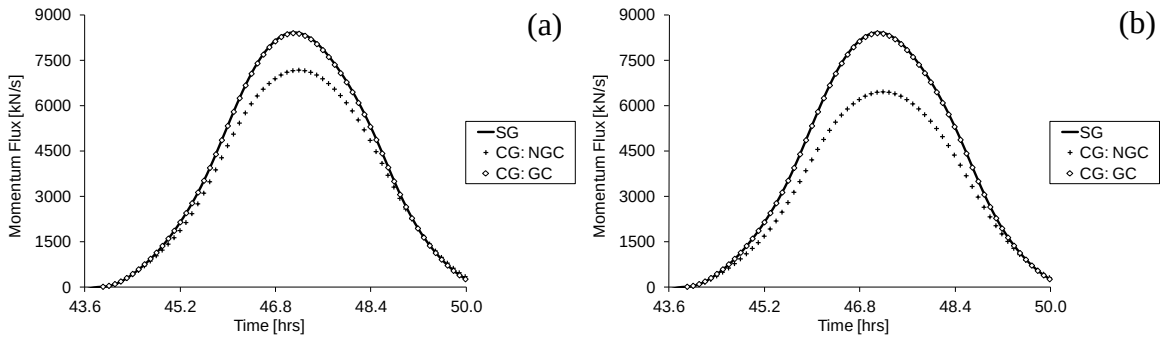

Figure 8: Comparison of incoming momentum flux across (a) CG1 interface and (b) the interface inside and adjacent to CG1.

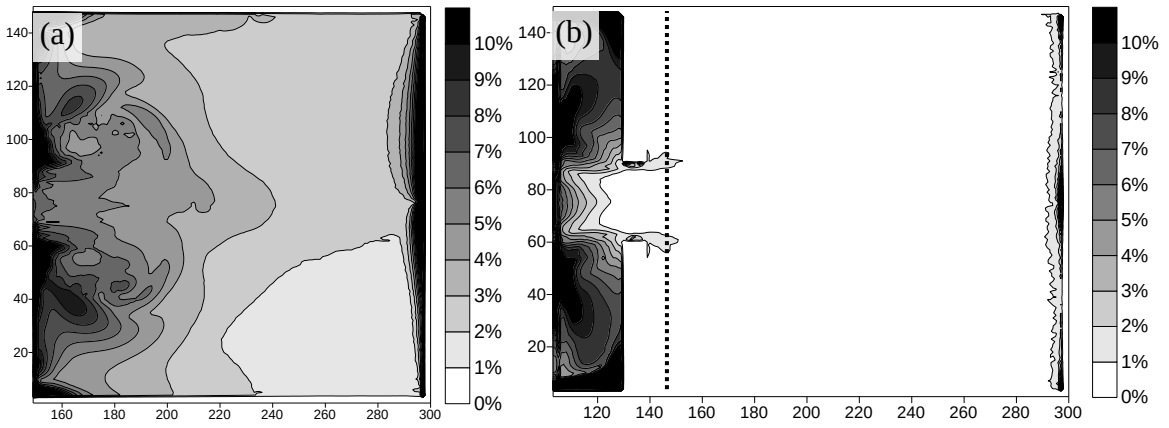

Figure 9: RE_T in CG current speeds for (a) CG1 simulation and (b) CG3 simulation (see Figure 5b for locations of CG1 and CG3). The AOI is the full extents of (a) and the area to the right of the dotted line in (b).

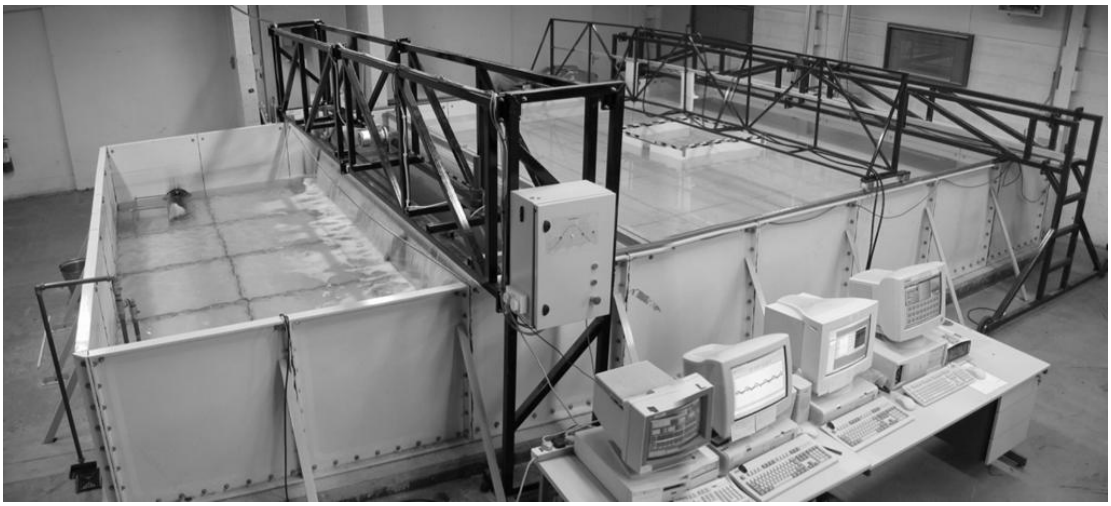

Figure 10: The tidal basin with the reservoir on the left and the working area on the right.

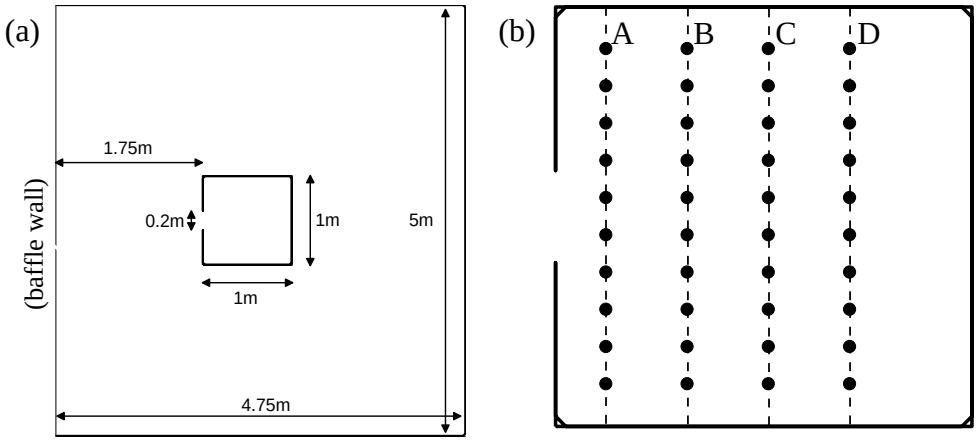

Figure 11: (a) Plan view o tidal basin working area and (b) velocity measurement points with AOI.

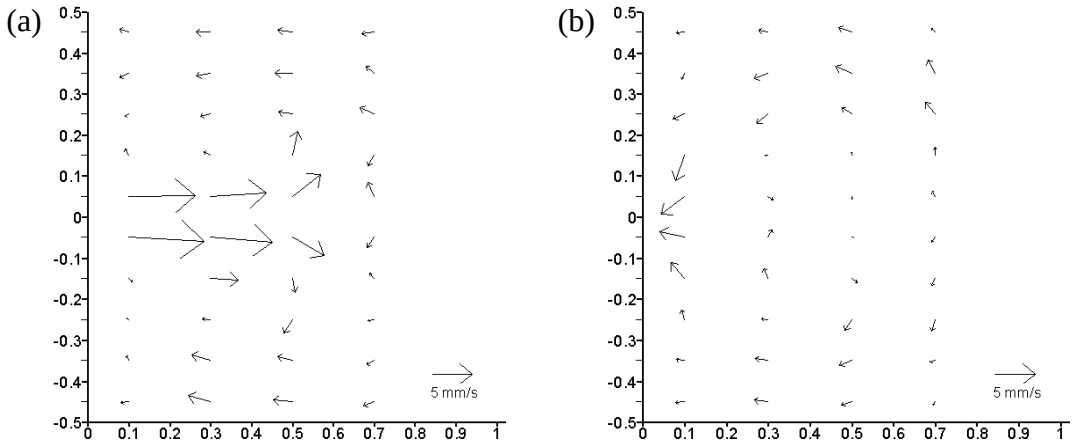

Figure 12: Measured transect velocities at (a) mid-flood and (b) mid-ebb.

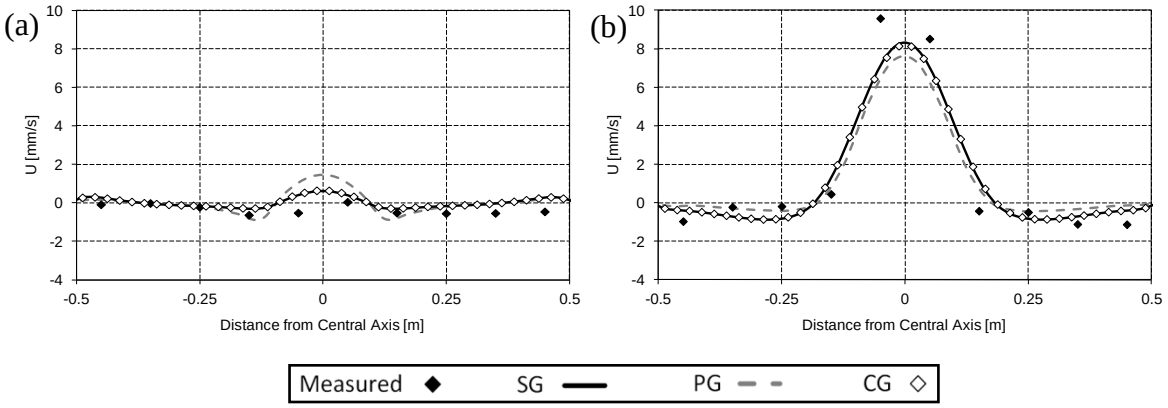

Figure 13: Comparison of x-direction current speeds along transect A at (a) low water and (b) mid-flood.

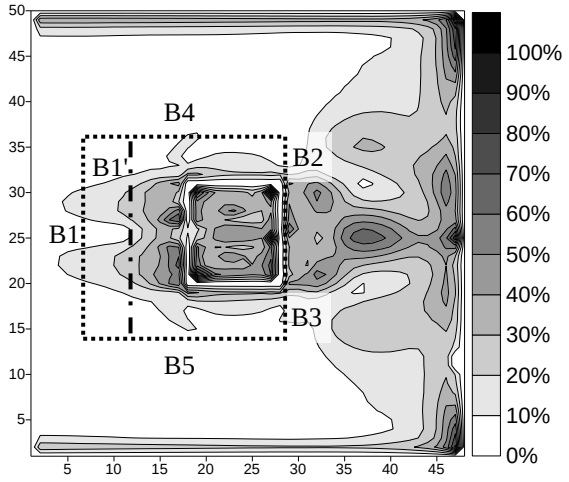

Figure 14: RE_T in PG current speeds relative to SG. Dashed lines show the CG boundary locations. The dash-dot line is an alternative boundary to B1.

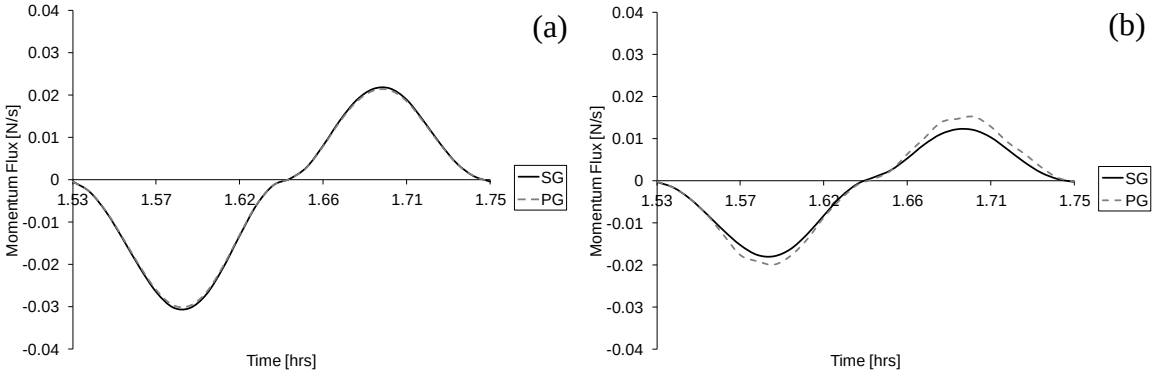

Figure 15: Comparison of PG and SG momentum fluxes across (a) the B1 boundary interface and (b) the B1' boundary interface (locations of B1 and B1' are shown in Figure 13).

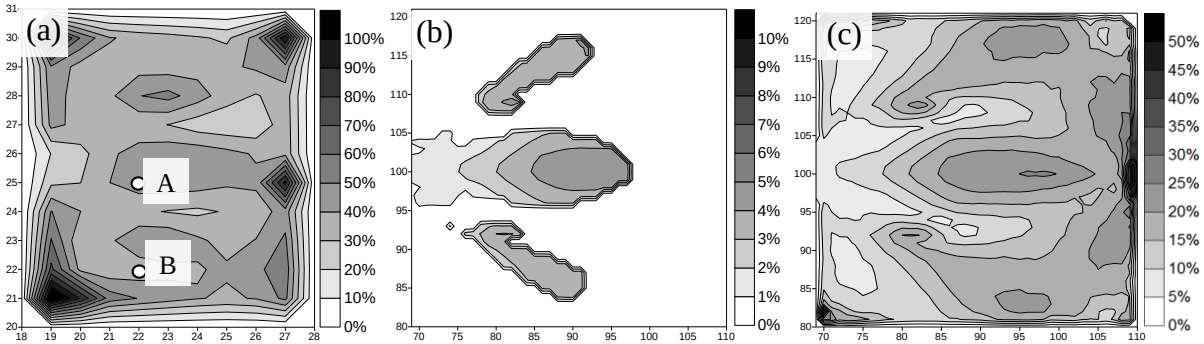

Figure 16: RE_T in current speeds in AOI for (a) PG, (b) CG using boundary B1 and (c) CG using boundary B1'.

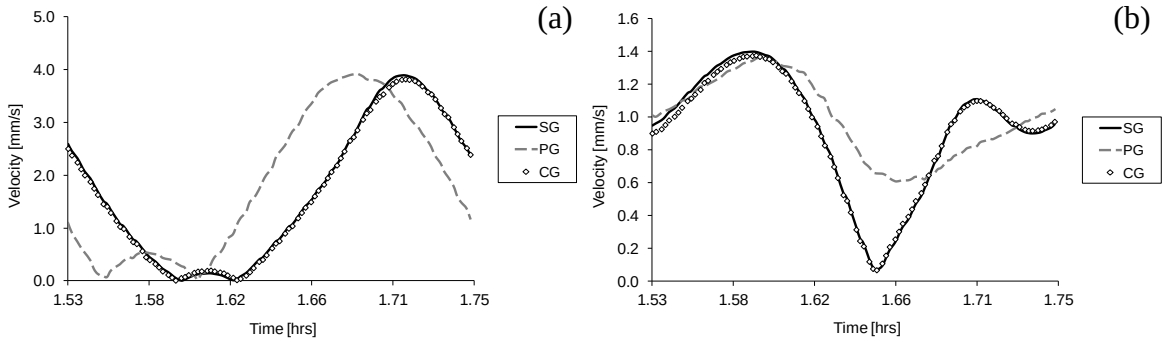

Figure 17: Comparison of current speeds at (a) Point A and (b) Point B (see Figure 10a for locations).

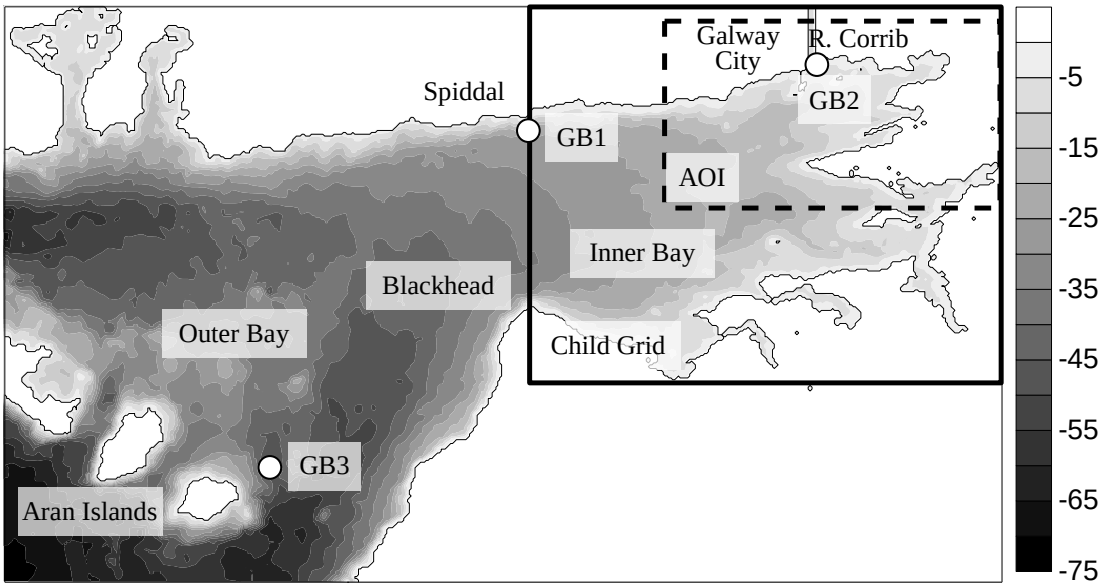

Figure 18: Galway Bay domain showing child grid, AOI (depths in m below spring high water) and measurement location GB1.

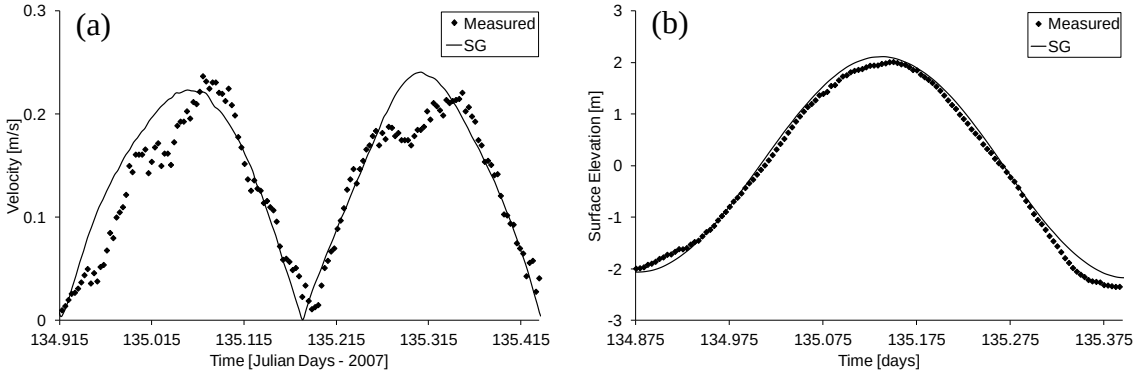

Figure 19: Comparison of (a) modelled and measured current speeds at GB1and (b) modelled and measured water surface elevations at GB2 (GB1 and GB2 are shown in Figure 17).

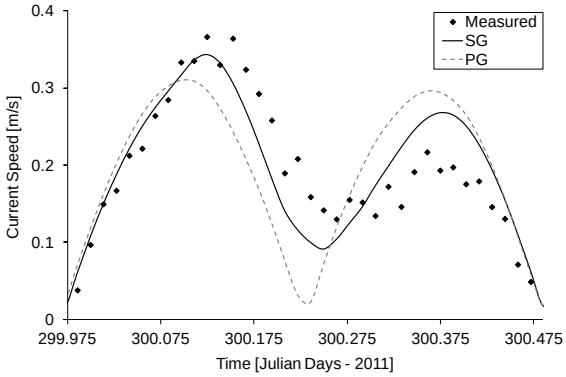

Figure 20: Comparison of modelled and measured current speeds at GB3.

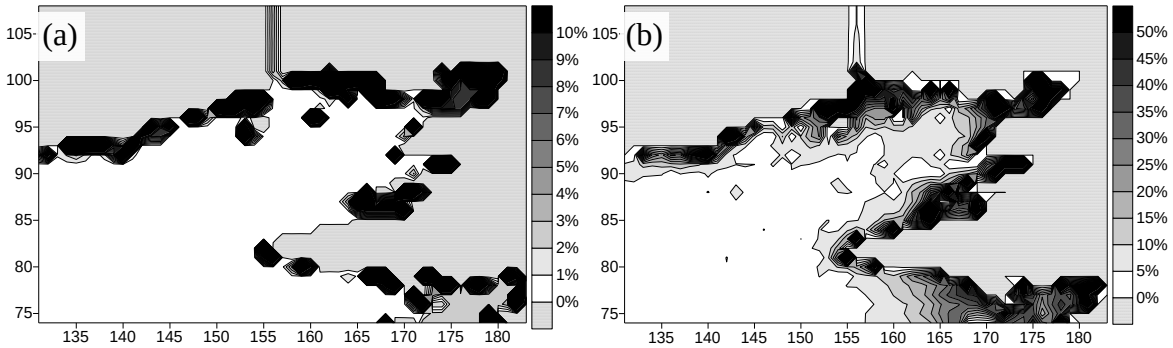

Figure 21: RE_T in PG solution for (a) elevations and (b) current speeds.

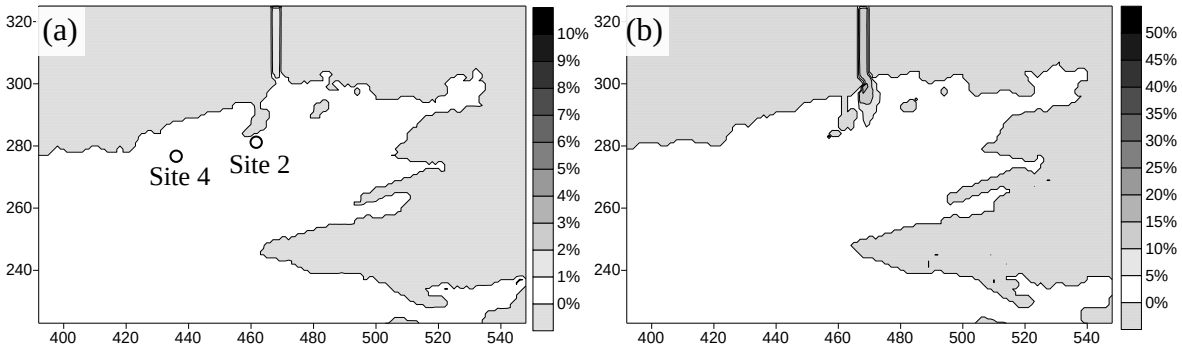

Figure 22: RE_T in CG solution for (a) elevations and (b) current speeds.

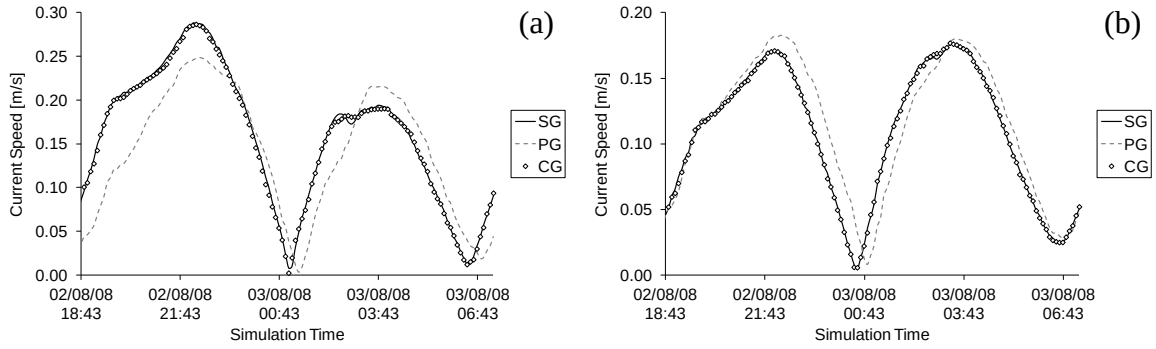

Figure 23: Comparison of current speed time series at (a) site 2 and (b) site 4.